Journal of Materials Science & Technology 250 (2026) 257–271

Contents lists available at ScienceDirect

Journal of Materials Science & Technology

journal homepage: www.elsevier.com/locate/jmst

Research Article

Biological skin-inspired damage warning and self-healing thermoelectric aerogel fiber via coaxial wet spinning for wearable temperature sensing

Hualing He[a], Qing Jiang[a], Yuhang Wan[a], Md Hasib Mia[a], Xueru Qu[a], Mi Zhou[a], Xingyu He[a], Xiaoqian Li[a], Min Hong[b], Zhicai Yu[a,*], Siqi Huo[b,*]

[a] State Key Laboratory of New Textile Materials and Advanced Processing, School of Textile Science and Engineering, Wuhan Textile University, Wuhan 430200, China
[b] Centre for Future Materials, School of Engineering, University of Southern Queensland, Springfield Central 4300, Australia

ARTICLE INFO

Article history:
Received 9 April 2025
Revised 9 June 2025
Accepted 12 June 2025
Available online 22 July 2025

Keywords:
Thermoelectric aerogel fiber
Coaxial wet spinning
Damage detection and warning
Self-healing
Multiple reversible bonds
Wearable temperature sensing

ABSTRACT

Biopolymer-based temperature-sensing fibers are increasingly employed to realize the eco-friendly concept of wearable electronics. However, keeping their long-term development remains challenging due to limited mechanical robustness and poor environmental tolerance. Herein, a bionic autonomous self-healing thermoelectric (TE) aerogel fiber with visual damage warning function (STDF) inspired by biological skin was prepared via a coaxial wet spinning strategy, which yielded a core-shell heterogeneous structure with a protective sheath with an intrinsic self-healing ability and a temperature-sensing core layer. The core layer of STDF, composed of flexible thermoplastic polyurethane embedded with rigid $Ti_3C_2T_x$ MXene, effectively minimizes disruptions in continuous conductive pathways during repeated extreme bending. Featuring a synergistic network of reversible hydrogen bonds and dynamic Schiff-base linkages constructed among oxidized alginate, sericin, and tannic acid, the fractured STDF aerogel fiber exhibits exceptional water-responsive self-healing efficiency (97.51 % stress recovery). Moreover, the visual damage location in STDF fiber is enabled through a coloration reaction at the damaged interface between the Fe^{2+} ions and 1,10-phenanthroline incorporated into the core and sheath layers, respectively. Furthermore, the resultant STDF demonstrates a wide-range temperature-sensing performance at 100–500 °C and an ultrasensitive alarm response time (within 2 s) when encountering fires. This work sheds new light on the design of bionic temperature sensing fibers with environment-adaptive self-healing and damage warning abilities for improved reliability and durability in real-world wearable application scenarios.

1. Introduction

Thermoelectric (TE) fiber-based generators are an attractive technology that enables noiseless and continuous direct heat-to-electricity conversion [1], which has led to remarkable progress in flexible wearable technologies [2], including energy harvesting [3,4], waste heat power generation [5], and temperature sensing [6–8]. In particular, flexible TE fiber-based self-powered temperature sensors have demonstrated strong potential for long-term continuous temperature monitoring in wearable electronics because of their truly breathable wearability properties, such as their dynamic surface conformability to the human body [9]. In contrast to active temperature sensors based on thermal resistance effects [10,11], TE fiber-based passive temperature sensors can directly convert temperature gradients into electrical voltage signals, thus achieving desirably long-term unattended temperature monitoring without frequent recharging. Hence, TE fiber-based passive temperature sensors have acquired autonomous environmental energy harvesting, signal transmission, and precise temperature perceptive functions and exhibit great potential to overcome the defects of resistance-type temperature-sensing electronic textiles. However, the emergence of nondegradable polymer-based TE temperature-sensing fibers has inevitably resulted in a serious ecological problem. Flexible TE fiber electronics based on natural materials and their derivatives have become increasingly able to realize the green and sustainability concepts, owing to their advantage

* Corresponding authors.
E-mail addresses: yuzhicaicai@163.com (Z. Yu), Siqi.Huo@unisq.edu.au, sqhuo@hotmail.com (S. Huo).

https://doi.org/10.1016/j.jmst.2025.06.038

of renewability and biocompatibility [12–15]. However, TE fiber-based temperature sensors based on biopolymers still have limitations because they typically lack mechanical adaptability to extreme conditions. The mechanical and functional performances of biopolymer fiber-based temperature sensors may fail after multiple stretches and bends during use, thereby affecting the lifespan of electronic devices [16]. Given this issue, developing new strategies to engineer biopolymer-based TE fibers with mechanical maneuverability, recoverability, and environmental tolerance to improve the reliability and durability of electronics is urgently needed.

Domestic and international scholars have made remarkable efforts in the field of self-healing fibers to address the above challenge. For example, they have introduced structures, like smart microcapsules and hollow fibers, to encapsulate repair agents within materials [17,18] or used self-healing coatings [19–21] to achieve self-healing ability when fibers are subjected to unexpected mechanical damage. Although extrinsic healing methods utilize repair agents to undergo chemical reactions or physical changes at damage sites to obtain reliable self-healing performance with high efficiency, they lose their repeatable healing performance when the repair agents are exhausted. Moreover, extrinsic healing methods employing self-healing agents or coatings do not allow for the preservation of the original fiber morphology after healing, i.e., they result in substantial changes in soft electronic morphology [22]. This situation leads to unstable fiber sensing performance, as well as the subsequent production of electronic fabrics that are not breathable, contradicting the original intention of using fibers to prepare soft and breathable temperature-sensing electronic textiles. By contrast, intrinsic self-healing fibers can achieve autonomous repeatable self-healing performance by combining the inherent reversibility of physical and chemical interactions [23–25] or by reconstructing hydrogen bonds and dynamic covalent bonds that break between damaged fiber interfaces [26–28]. Therefore, biomass-based TE fibers with autonomous intrinsic self-healing ability show promising potential in wearable temperature-sensing electronics.

However, an important problem with intrinsically self-healing fibers in practical applications is that cracks generated by wear or impact can expand the failure zones of functional fibers due to fatigue propagation, leading to a reduction in fiber durability [16]. The propagation of functional failure areas can be suppressed if surface microcracks can be detected promptly and prevented from expanding by crack healing [29–31]. Moreover, endowing damage warning performance to self-healing TE fibers allows electronic fibers to detect damage in a timely manner at an early stage and recover their reliable sensing performance by manually providing self-healing driving conditions (i.e., temperature, moisture, pressure, and illumination) and thus prolongs service life. Therefore, proposing an effective strategy for TE fiber-based temperature sensors that can simultaneously detect defects and repair cracks is an attractive but challenging goal. In the natural world, biological systems can solve the above problem well due to their strong adaptive performance. For example, after an external injury, human skin first transmits pain signals to the brain via sensory neurons, and bleeding occurs at the local injury site for spontaneous damage warning. Subsequently, the damaged skin undergoes three repair processes: inflammation, cell proliferation, and tissue regeneration. The integration of a self-alarm function in TE fibers ensures that fiber sensors' damage information or functional degradation events of fiber sensors are communicated in time, and their mechanical and functional properties are subsequently recovered through autonomous self-healing. To this end, we introduce the dual capabilities of damage defect visualization and self-repair through multiple dynamic bonds into temperature-sensing TE fibers to realize the desired reliability and durability.

Herein, inspired by biological skin, a bionic self-healing TE aerogel fiber with visual damage warning function (STDF) was prepared via a facile and cost-efficient coaxial wet spinning strategy, which yielded a core-shell heterogeneous structure with an intrinsic self-healing protective sheath and a temperature-sensing core layer. Specifically, we integrated the dynamic polymers oxidized sodium alginate (OSA), silk sericin (SS), and tannic acid (TA) into a sodium alginate (SA) biopolymer backbone to form a self-healing protective shell with multiple reversible bonds (reconfigurable hydrogen bonds and dynamic covalent bonds) that provide recoverable temperature sensing performance under various forms of damage. The core layer of STDF is composed of flexible thermoplastic polyurethane (TPU) embedded with rigid $Ti_3C_2T_x$ MXene, which effectively mitigates the interruption of continuous MXene conductive paths under repeated limit bending. Simultaneously, the incorporation of Fe^{2+} and 1,10-phenanthroline (Phen) into the core and sheath layers confers STDF fiber with visual damage detection capability because of the coloration reaction between Fe^{2+} and Phen at the damage interface. The resulting STDF exhibits reversible mechanical behavior from cutoff status with a remarkable self-healing efficiency of 97.51 % in strength under water-driven conditions at room temperature. Furthermore, due to the direct correlation between the voltage generated and the temperature difference, STDF showcases precise temperature-sensing abilities across a broad range (100–500 °C). This indirectly highlights its potential for providing high-temperature alert capability for firefighting clothing before the protective clothing's thermal degradation in fire cases. The bionic autonomous self-healing property and damage self-detection capability reported herein can pave the way for delivering next-generation eco-friendly and durable temperature-sensing TE fibers with wide application potential in textile electronics.

2. Experimental section

2.1. Materials

Phen (98 %) was purchased from Bide Pharmatech Co., Ltd., China. TPU (1170A, BASF) was purchased from Sigma Aldrich Co., Ltd., China. SA (Mw = 2.7×10^5), sodium periodate ($NaIO_4$), calcium chloride ($CaCl_2$), sodium chloride (NaCl), hydrogen chloride (HCl), ethylene glycol (EG), Ethanol absolute, ferrous sulfate (Fe_2SO_4), dimethyl sulfoxide (DMSO), silver nitrate ($AgNO_3$), poly(vinylpyrrolidone) (Mw = 1300,000) and iron (III) chloride ($FeCl_3$) were purchased from Sinopharm Chemical Reagent Co., Ltd., China. SS and titanium aluminum carbide (Ti_3AlC_2, 200 mesh, ≥ 98.0 %) were purchased from Shanghai Macklin Biochemical Technology Co., Ltd., China. Lithium fluoride (LiF; AR) and TA (Mw = 1701.20) were purchased from Shanghai Aladdin Biochemical Technology Co., Ltd., China. All pharmaceutical reagents were utilized as supplied, and deionized water was employed in all experiments.

2.2. Preparation of OSA

Initially, 4 g of SA was dissolved in 200 mL of distilled water to create a 2 wt. % SA solution. Then, 2.4 g of $NaIO_4$ was introduced to this SA solution, and the reaction was maintained at 30 °C in the absence of light. After 24 h, 0.8 mL of EG and 1.2 g of NaCl were added to the mixture, which was then stirred continuously for 30 min to complete the oxidation reaction. The resulting precipitate was extracted using ethanol and subsequently washed three times with distilled water to purify it. Ultimately, the white precipitate of OSA was obtained through freeze-drying.

2.3. Preparation of Ag NWs

In this study, Ag NWs were successfully synthesized using a standard polyol method. Initially, 20 mL of EG was heated in an oven at 160 °C for 1 h, then allowed to cool to 47.6 °C. Subsequently, 0.1 g of $FeCl_3$ and 0.052 g of PVP were dissolved in the cooled EG solution and stirred in an oil bath for 1.5 h. Thereafter, 0.724 g of $AgNO_3$ was added to the mixture and stirred for 10 min until fully dissolved. The solution was then placed in an oven at 180 °C for 7 h until a gray dispersion formed. After cooling to room temperature, the dispersion was collected through centrifugation and washed several times with ethanol to yield pure Ag NWs.

2.4. Preparation of MXene nanosheets

The MXene nanosheet dispersion was prepared by acid-etching Ti_3AlC_2 powder using an HCl/LiF mixture, following a standard preparation protocol. First, an etching solution was made by mixing 1.6 g of LiF with 20 mL of 12 mol/L HCl, which was then magnetically stirred for 40 min. Subsequently, 1.6 g of Ti_3AlC_2 was added to this solution, and the mixture was stirred thoroughly for 24 h to ensure the complete removal of the aluminium layers. The resulting dispersion was washed extensively with distilled water through centrifugation at 3000 r/min for 10 min until the pH of the supernatant exceeded 6. This MXene precipitate was then subjected to ultrasonic washing for 2.5 h, followed by another centrifugation at 3000 r/min to isolate a monolayer of the MXene nanosheet dispersion. Finally, the required MXene nanosheets were collected through freeze-drying, intended for use as the spinning dope in the core layer of the core-sheath TE fiber.

2.5. Preparation of the coaxial-structured STDF

Initially, 0.1 g of TPU particles were combined with 10 mL of DMSO solvent and stirred for 3 h to prepare a TPU solution. Thereafter, MXene (50 mg/mL), Ag NWs (10 mg/mL), and Fe_2SO_4 (10 mg/mL) were incorporated into the TPU solution to form the core spinning solution. Subsequently, SS (1 g), OSA (1 g), and SA (0.3 g) were mixed with 10 mL of deionized water to prepare the shell spinning dope. The core and shell spinning dopes were then injected into the inner and outer coaxial needles using separate syringe pumps. The inner (22 gauges; inner diameter: ~0.41 mm) and outer (14 gauges; inner diameter: ~1.60 mm) needles were set to an injection speed of 500 μL/min. Following this, the coaxial spinning solution was transferred into a 10 mL syringe and spun into an aqueous coagulation bath with 4 wt. % $CaCl_2$ to create a Ca^{2+} cross-linked nascent STDF hydrogel fiber. Subsequently, part of the water in the nascent STDF hydrogel fiber was replaced through solvent exchange with a 30 % EG solution. The fiber was then soaked in varying concentrations (0.1 wt. %, 0.2 wt. %, and 0.3 wt. %) of a TA aqueous solution. After that, the fiber was frozen at −20 °C and freeze-dried for 24 h to produce STDF aerogel fiber. Finally, the surface of the STDF aerogel fiber was sprayed with a Phen (10 mg/mL) aqueous dispersion, leading to the development of ultralight STDF with a core-shell structure (diameter: ~1.16 mm; linear density: ~102.86 tex).

2.6. Fabrication of SFET

Following the aforementioned STDF preparation method, the size of the spinning needle with a 22-gauge inner needle (inner diameter: ~0.41 mm) and a 17-gauge outer needle (inner diameter: ~1.04 mm) was changed to acquire fine fibers. The resulting SFET was fabricated by sewing the prepared fiber (length = 7.43 cm, diameter = 0.75 mm) flat onto commercially available aramid fabric (length = 8.45 cm, width = 3.01 cm).

2.7. Material characterization

Fourier Transform infrared spectroscope (FTIR, TENSOR 27, Bruker, Germany) and X-ray photoelectron spectroscope (XPS, Thermo Scientific K-Alpha, USA) were utilized to analyze the chemical composition of the samples. X-ray diffraction (XRD) was performed with a Rigaku XRD instrument (Japan). To characterize the structure and micromorphology, a scanning electron microscope (SEM, MVE016, Phenom, Netherlands) and an energy-dispersive X-ray spectroscope (EDX, JSM-IT500A, Japan) were employed. Tensile tests were carried out using a universal material testing machine (Instron 3365, USA) at a stretching rate of 100 mm/min. Cyclic mechanical properties were evaluated with a flexible material multimodal tester (Suzhou Shengte Intelligent Technology Co., Ltd.). The electrical resistance and voltage of the coaxial TE fiber samples were measured with a digital multimeter (UT61E+, China). The flame retardancy of the fiber samples was assessed using an intelligent critical oxygen index analyzer (Tech-GBT2406–1, China). Thermal stability was analyzed through thermogravimetric analysis (Mettler Toledo, USA) from 30 to 800 °C at a heating rate of 10 °C/min under a nitrogen environment. The combustion behavior of the samples was characterized using a microscale combustion calorimeter (MCC-2, Govmark, USA) following ASTM D7309–2007. An infrared thermal camera (DM-I220, China) was employed to record surface temperatures and observe the temperature distribution of the coaxial TE fiber samples during the heating phase.

2.8. Thermal degradation kinetics analysis

The kinetic parameters obtained using the Kissinger and Flynn Wall Ozawa methods were further analyzed for the thermal degradation behavior of STDF. The activation energy (E) represents the minimum energy required for a chemical reaction during thermal decomposition and is a key parameter for characterizing the kinetics of thermal degradation. The Kissinger method is a simple way to roughly estimate the value of E. This study initially used the method to determine E based on the temperature related to the peak thermal degradation rate in the differentiation thermogravimetry (DTG) curves obtained at different heating rates. For this method, use Eq. (1) to calculate the E value:

$$\ln\left(\frac{\beta}{T_m^2}\right) = -\frac{E}{RT_m} + \ln\left(\frac{AR}{E}\right) \tag{1}$$

where β represents the heating rate (K/min), T_m denotes the thermodynamic temperature at the peak thermal weight loss rate (K), E refers to the activation energy (kJ/mol), R is the gas constant (8.314 J/mol^{-1} K^{-1}), and A signifies the pre-exponential factor. By determining the fitting line of $\ln(\beta/T_m^2)$ against $1/T_m$, we can calculate E and the pre-exponential factor A using the slope and intercept of the line [32,33]. The Flynn-Wall-Ozawa method utilizes TG curves obtained at various heating rates to determine E, as illustrated in Eq. (2):

$$\ln\beta = \ln\left(\frac{AE}{R}\right) - \ln F(\alpha) - 5.3305 - 1.052\frac{E}{RT} \tag{2}$$

where $F(\alpha)$ represents a specific conversion function that mirrors the reaction model, where α denotes the conversion value, β indicates the heating rate (K/min), and T refers to the thermodynamic temperature (K). The $\ln\beta$ versus $1/T$ graph forms a straight line, and the slopes of these fitted lines are utilized to determine the apparent activation energy.

3. Results and discussion

3.1. Designation and construction of biological skin-inspired STDF fiber

Biological skin, a sensory organ for the interaction with the external environment of the human body, possesses a structure that endows the ability to perceive various stimuli from the outside world keenly, as well as provides astonishing damage self-detection and repair abilities, enabling the skin to bear the responsibility of protecting the body from external harm [34]. Human skin has a tissue structure that consists of the epidermis, dermis, and subcutaneous tissue; the regenerative epidermis is located in the outermost layer of the skin, whereas the dermis is located deep within the epidermis and has blood vessels and nerves but lacks regenerative ability [35]. The skin epidermis can warn of bleeding and quickly restore its integrity when damaged, thereby preventing harmful substances from further invading the dermis layer and avoiding considerable damage to the dermis layer. This ability provides the inspiration for our design and preparation of core-sheath TE fibers (Fig. 1(a)). In this work, inspired by human skin, we designed STDF with a core-sheath heterogeneous structure and autonomous self-healing and damage detection functions by using microfluidic-assisted coaxial wet spinning technology. This fiber includes a protective sheath with an intrinsic self-healing ability and a temperature-sensing core layer (Fig. 1(b)). To obtain the spinning solution of the ultrasensitive temperature-sensing core layer, the Al layers in precursor Ti_3AlC_2 were usually removed by etching with fluoride salt and hydrochloric acid, followed by centrifugation and ultrasonic treatment to prepare MXene nanosheets (Fig. S1(a) in the Supplementary Materials). The SEM images of MXene under different magnifications in Fig. S1(b) and (c) indicate the successful exfoliation of MXene nanosheets. Fig. S2 illustrates that the (002) diffraction peak of MXene appears at a lower angle (5.42°) compared to Ti_3AlC_2 (9.4°), indicating the successful synthesis of MXene [36]. Furthermore, the crystal faces of (004), (101), and (104) have disappeared entirely after etching and delamination. Subsequently, MXene nanosheets were mixed with silver nanowires (Ag NWs) prepared through the polyol method, Fe^{2+}, and TPU/ DMSO solution through magnetic stirring to obtain the spinning solution as the core material (Fig. 1(c)). The introduction of Ag NWs connected each 2D layered MXene structure, thereby constructing a continuous 3D interconnected conductive network in STDF fibers [37] (Fig. S3). Meanwhile, compared with other organic solvents, such as N, N-dimethylformamide, DMSO can better intercalate into MXene layers to achieve high dispersibility [38], thereby constructing continuous conductive pathways. The TPU/MXene-constructed core layer (abbreviated as “core”) in STDF endows elasticity and structural deformability that help improve conductive stability when confronted with bending.

The spinning solution of the protective sheath of STDF was prepared following our previous method [39]. SS cross-linked OSA with efficient imine bonds was intentionally embedded into the SA matrix to provide room-temperature self-healing ability, which is crucial for the self-healing of the shell layer in the self-healing TE fiber (Fig. 1(d)). Subsequently, the STDF fiber precursor in the hydrogel state was alternately immersed in a solution of calcium chloride ($CaCl_2$, 4.0 wt. %) and TA (0.2 wt. %). Finally, the Phen aqueous dispersion was evenly sprayed on the above-mentioned freeze-dried fiber to obtain STDF with autonomous self-healing and damage detection capabilities. STDF contains approximately 30 wt. % SA as a flexible chain for entropy elasticity and a high concentration of $CaCl_2$ as a hygroscopic and ionic cross-linking agent. Increasing the $CaCl_2$ content from 2 wt. % to 4 wt. % remarkably increases the resulting cross-link density of STDF. The -OH of TA in the protective sheath of the STDF fiber can form numerous dynamic hydrogen bonds with the -OH and -COOH groups of SA and the $-NH_2$ groups of SS, creating a complex cross-linked network through the interaction of multiple hydrogen bonds [40].

The specific surface area (SSA) and pore size distribution of the as-prepared core-sheath STDF fiber were evaluated by using N_2 adsorption-desorption curves. As presented in Fig. 1(e), the adsorption isotherm of STDF fibers belongs to the typical IV type isotherm, which exhibits an H2b hysteresis loop at a relative pressure of 0.4–1, reflecting the presence of a large number of ordered mesoporous structures. Furthermore, the width of the hysteresis loop is relatively narrow, suggesting that the fiber has a relatively uniform pore size distribution and consistent pore size, indicating excellent structural orderliness [41]. The same result is also obtained for the core fiber, as shown in Fig. S4 and Table S1. Moreover, STDF and the core fiber (fibers spinning using STDF core materials alone) have SSA values of approximately 13.14 and 12.92 m^2/g, respectively, as acquired through the Brunauer-Emmett-Teller method, and the mean pore diameters of 3.59 and 2.45 nm, respectively (Fig. S5). As presented in Fig. 1(f) and Table S2, five aspects, including healing efficiency, damage detection, limiting oxygen index (LOI), knittability, and flexibility, were evaluated to highlight the superiority of the prepared STDF aerogel fiber over existing high-performance functional fibers. The results show that among the fibers, the STDF aerogel fiber has the highest LOI (~38 %) and best comprehensive healing efficiency and damage monitoring ability. Therefore, the prepared STDF aerogel fiber has potential application prospects in the production of wearable high-temperature warning sensors due to its unique advantages of light weight, flame retardancy, and excellent wear resistance on dynamic body curves.

3.2. Morphology and structure of STDF fiber

Chemical bonding between OSA and the coaxial STDF fiber protective shell (abbreviated as “shell”) was investigated through XPS, as shown in Fig. 2(a–c). The survey scan XPS spectrum of the as-prepared shell fiber (fibers spinning using STDF sheath materials alone) exhibits typical peaks of C 1*s*, O 1*s*, N 1*s*, and Ca 2*p* at 285, 532, 399, and 347 eV, respectively, verifying the formation of calcium complexes in the fibers after spinning and forming [42] (Figs. 2(a) and S6). Furthermore, the detailed scan XPS C 1*s* spectrum of OSA contains a sharp $C = O$ peak at 289 eV, confirming the presence of aldehyde groups (Fig. 2(b)). Meanwhile, FTIR reveals the presence of typical absorption bands at 1732 and 2933 cm^{-1} corresponding to the symmetrical vibrational absorption peaks of aldehyde carbonyl groups, indicating that SA has been successfully oxidized to form OSA with aldehyde groups [43,44] (Fig. S7). In addition, a deconvolution peak at 285.8 eV in the high-resolution C 1*s* spectrum of the shell is attributed to $C = N$, confirming the basis for the formation of Schiff base bonds (Fig. 2(c)).

The interface interaction between the core and shell layers was studied using FTIR. STDF exhibits all characteristic peaks of the combination of the pure shell and core fibers (Fig. 2(d)), including the vibration absorption peaks of MXene at 3394 and 1124 cm^{-1} corresponding to -OH and C-O in the core fiber (Fig. S8(a)), as well as the absorption peak of 1590 cm^{-1} corresponding to C=N in the shell fiber (Fig. S8(b)). Moreover, the FTIR spectrum of the fiber shows a shift in the peak at 3500 cm^{-1} corresponding to -OH, which may be due to the presence of MXene in the core. Afterwards, the effect of TE materials on the crystal structure was evaluated through an XRD test. As shown in Fig. 2(e), the peak intensity in XRD of STDF fiber containing MXene is enhanced, indicating that the MXene in the core is effectively introduced into the coaxial-structured STDF fibers. Additional peaks appear in XRD after the oxidation of SA, due to the breakage of SA molecular chains

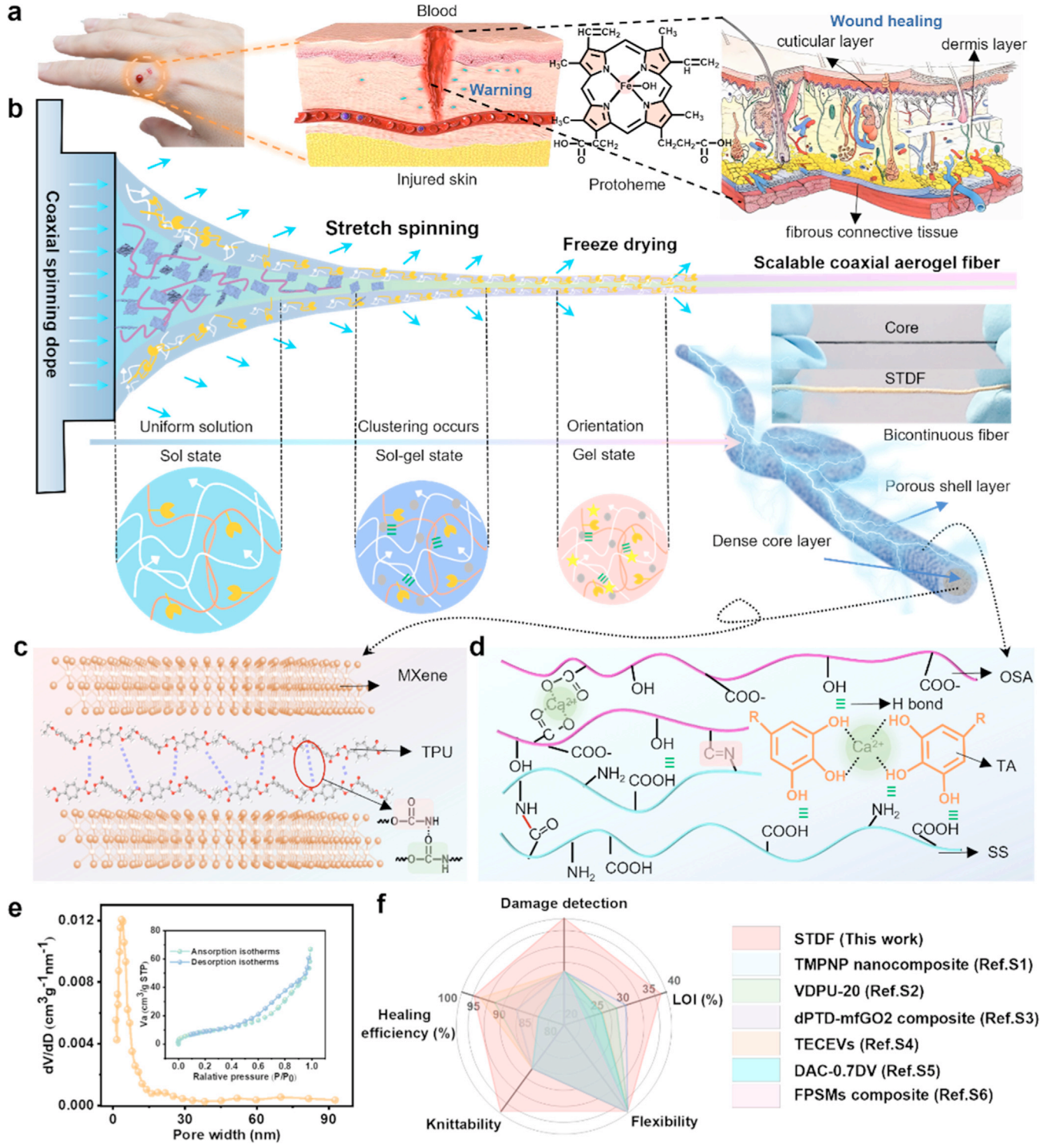

Fig. 1. Design concept and preparation of biomimetic STDF fiber with self-healing and damage warning abilities. (a) Schematic of the bleeding and self-healing characteristics of damaged human skin. (b) Schematic of microfluidic-assisted coaxial wet spinning for the fabrication of STDF fiber with high-density hydrogen bond groups and Schiff base bonds embedded in the SA matrix. (c) MXene enhances the mechanical properties of polyurethane and the self-association of TPU segments. (d) Schematic of the cross-linked TA network structure and self-healing mechanism of the OSA composite with SS in STDF. (e) N_2 adsorption-desorption curve and pore size distribution of STDF fiber. (f) Comprehensive comparison of the sensing, self-healing, and mechanical properties of STDF and other self-healing fibers.

caused by the oxidation reaction, resulting in short molecular fragments arranged and stacked in different ways to form new crystal structures (Fig. S9(a)). Fig. S9(b) shows that the XRD peaks of STDF are not prominent, due to the similar diffraction peaks of its various components, resulting in overlapping and indistinguishable peaks in the XRD pattern. However, the successful preparation of STDF fiber with a porous shell and dense core layer is clearly seen in Fig. 2(f). The porous shell can absorb and disperse external impact energy to a certain extent, thereby improving the toughness of the fiber. Dense cores have high density and a tight atomic or molecular arrangement, achieving the 3D bridging effect of the prepared Ag NWs (Fig. S10(a) and (b)) on MXene. This structure

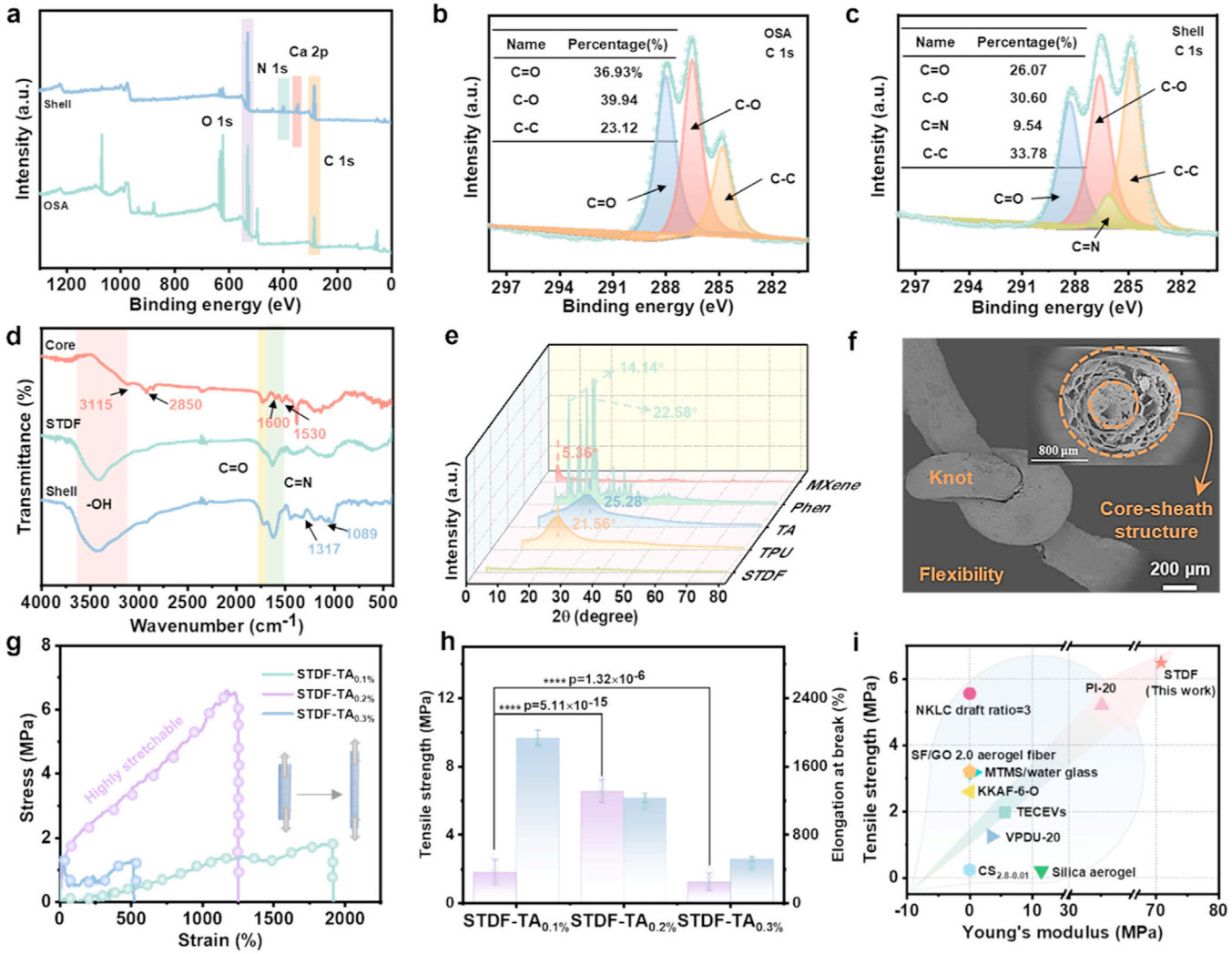

Fig. 2. Structural and compositional characterizations of biomimetic STDF fiber. (a) XPS survey scan and C 1s of (b) OSA and (c) the shell fiber. (d) FTIR spectra and (e) XRD patterns of the shell fiber and STDF. (f) High-resolution SEM image of STDF. (g) Representative stress-strain curves of STDFs with different TA concentrations. (h) Statistical ultimate tensile strength. Asterisks denote statistical significance: $^{****}p < 0.0001$. (i) Comparison of the tensile strengths and Young's moduli of STDF and other self-healing fibers.

makes the fiber less prone to breakage when subjected to impact and can maintain good integrity.

To investigate the macroscopic effect of TA on multiple hydrogen bonds in STDF fibers, we tested the mechanical properties of STDF fibers at different concentrations of TA. The strengths of the STDF samples cross-linked by different TA concentrations vary. The experimental results show that the strength of the fibers exhibits a linear increasing relationship when the TA content is 0.1 wt. % and 0.2 wt. %. This is because an appropriate amount of TA can enhance the tensile strength and elastic modulus by strengthening the internal or interfacial bonding forces of fibers (such as hydrogen bonding or cross-linking). However, when the TA content increases to 0.3 wt. %, this increasing relationship is not satisfied. Excessive TA leads to excessive cross-linking or agglomeration within the fibers, resulting in stress concentration points and ultimately reducing strength and modulus. Therefore, a concentration of 0.2 wt. % concentration of TA is the optimal parameter, which helps to crosslink and fuse shell fibers, facilitating their penetration without damaging the biomolecules' structure. Subsequently, coaxial fibers with a double continuous interlocking structure with a strength of up to 7 MPa are produced (Fig. 2(g, h) and Table S3). The resulting tensile strain can reach 1250 % due to the super elasticity and uniform interface of the inner layer of the superelastic polyurethane fibers. As shown in the cross-sectional SEM image, the self-healing fiber has a core-shell structure, exposing two porous fiber layers. After knotting, the double-layer structure deforms synergistically without interlayer delamination or fiber pull-out (Fig. 2(f)). This finding indicates that the abundant functional groups on the surface of MXene are closely related to the strong interfacial adhesion of SA. These results indicate that STDF fiber has excellent mechanical strength and broad application prospects in wearable electronic fabrics compared with other existing TE fibers reported in the literature (Fig. 2(i) and Table S4).

3.3. Damage warning and self-healing performances of STDF fiber

The mechanism of biological injury and bleeding is extremely complex. Foreign microorganisms, such as bacteria or other physical and chemical factors, can invade the cell membrane of an organism. Cell membrane damage can cause disorder in the exchange of substances inside and outside cells, leading to cell damage (Fig. 3(a)). This type of mechanical injury can cause the rupture of blood vessel walls within the skin, allowing blood to flow out of blood vessels and warning of biological damage (Fig. 3(b) and (c)). Platelets accumulate at the wound site and release clotting factors and fibrinogen, forming blood clots to seal damaged

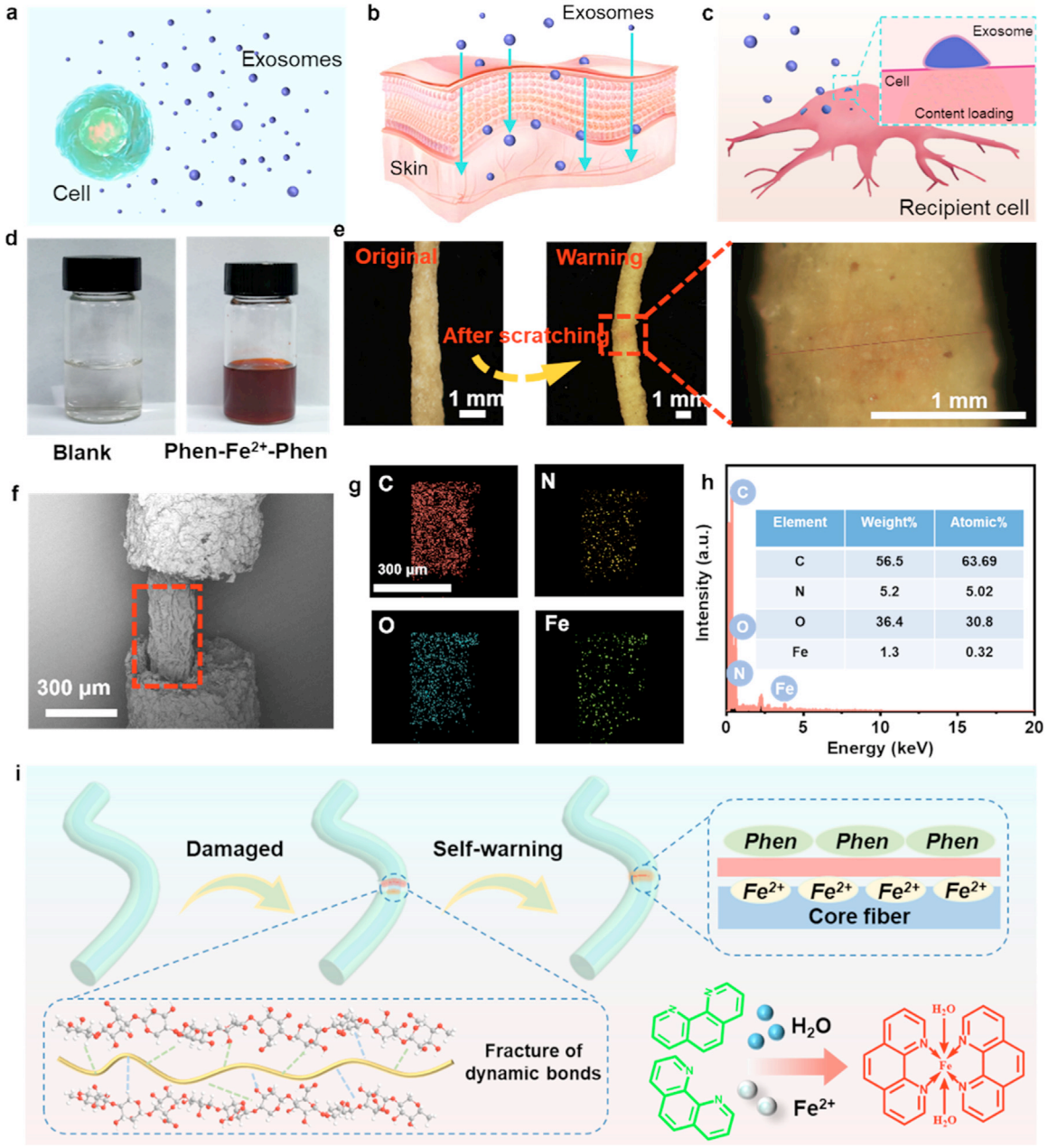

Fig. 3. Damage warning performance of STDF inspired by biological skin. (a–c) Schematic of the bleeding and healing mechanism of biological injuries. (d) Photo of the orange complex formed between Phen and Fe^{2+}. (e) Microscope images of damage warning by STDF. (f) SEM images of the coaxial-structured STDF. (g) EDX mapping images of C, O, N, and Fe in STDF. (h) EDX spectrum of STDF. (i) Schematic of the protective mechanism of the biomimetic STDF with self-healing and damage-sensing properties.

blood vessels. Through an inflammatory response, cells and factors jointly clear bacteria, foreign bodies, and necrotic tissue inside wounds, creating conditions for subsequent healing. Inspired by this mechanism, a heme-like structure was developed that forms a stable five-membered chelating ring based on the reaction of Phen with Fe^{2+} (Fig. 3(d)). A core-shell fiber structure was designed, inspired by the architecture of biological skin tissue. Under water-driven conditions, the damaged core-sheath fiber can clearly show red scratches under the microscope due to the rapid reaction between Fe^{2+} in its inner layer and Phen in its outer layer, generating stable orange-red compounds (Fig. 3(e)). Elemental analysis was conducted on SEM images for detailed observation (Fig. 3(f)). As shown in Fig. 3(g) and (h), the outer shell of the STDF core-shell fiber is peeled off and to observe the elemental distribution on the surface of the core layer. Fe elements are evenly distributed in the core layer, providing a basis for visual damage warning and localization. Therefore, when the fiber is damaged, the affected area can be quickly located visually, minimizing the adverse effects caused by fiber damage.

The protective mechanism of the biomimetic STDF is depicted in Fig. 3(i). First, Phen is an appropriate indicator, with its three-ring conjugation forming a strongly rigid planar structure and a robust conjugation system. Hence, the electron density of N on the aromatic ring increases, and the transfer of electron energy is promoted. Once the shell is broken, various reversible bonds (hydrogen and Schiff base bonds) within the shell can facilitate self-healing of damage, restore the protective function of the shell, and ensure its safety. In addition, when the shell is damaged, the external Phen can complex with the generated Fe^{2+}, and the color of the wound changes from yellow to red within a few seconds of

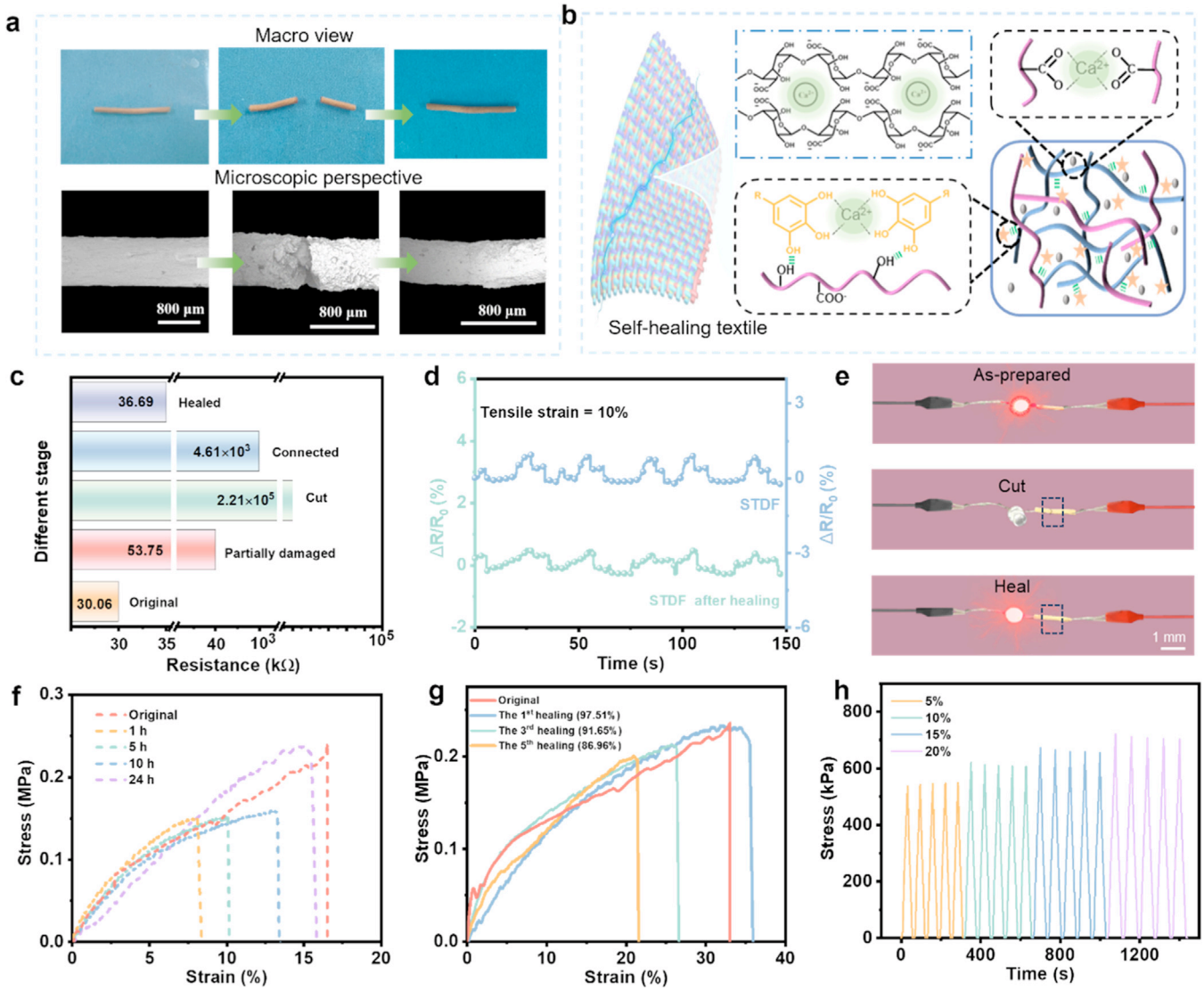

Fig. 4. Demonstration of STDF's autonomous self-healing capability. (a) Autonomous self-healing scar observed within 24 h at room temperature (RH 20 %–40 %) through optical and SEM imaging. (b) Schematic of the chemical structure of STDF. (c) Electrical resistance changes of STDF at different stages from damage to healing. (d) Resistance change rate curves of STDF after five times of cyclic stretching before and after healing (tensile strain of 10 %). (e) During healing, STDF makes the LED light glow (external power supply is 6 V). (f) Stress-strain curves of STDF at different healing times. (g) Mechanical performance of STDF after different healing cycles. (h) Stress changes in STDF after five cycles under different strains of 5 %, 10 %, 15 %, and 20 %.

contact with Fe^{2+} to enable visual observation and warn of the occurrence of damage, hence realizing the independent early warning of shell damage. With the defect warning function and repair capability of the shell, the protection life of the biomimetic coaxial STDF is greatly extended. Multifunctional biomimetic fibers with superior protective capabilities, self-healing properties, and active damage warning systems deserve more selection than the previously designed intelligent fibers. The design of the bionic STDF greatly expands its practical application prospects in protection fields, such as flexible electronic textiles.

As a result of the molecular properties of STDF, TE devices based on STDF exhibit rapid self-healing even without external stimuli at room temperature. STDF demonstrates remarkable self-healing capabilities in terms of mechanical and electrical properties. As shown in Fig. 4(a), scratch testing was conducted under an electron microscope. The optical and electron microscope images are consistent, showing that the disconnected STDF fully heals within 24 h at room temperature (relative humidity (RH) 20 %–40 %). The Schiff base bonds used in this study are well-known reversible dynamic bonds demonstrating effective exchange reactions activated at room temperature. When damaged, these Schiff base bonds trigger a reaction mechanism driven by water, enabling self-repair. It was observed that the STDF structure forms Schiff base bonds by cross-linking SS with OSA. At the same time, hydrogen bonding between TA and SA achieves double-bond healing, significantly improving the self-healing efficiency of STDF (Fig. 4(b)).

Fig. 4(c) illustrates the changes in the resistance of the STDF fiber during water-driven self-healing. When fiber damage occurs everywhere in a water environment, the fiber is activated, causing internal dynamic covalent bonds to continuously break and rebuild in damaged areas. Subsequently, new hydrogen and Schiff base bonds form to repair cracks when dynamic equilibrium is reached. Additionally, the electrical resistance of a 16.42 mm-long STDF sample (1.13 mm in diameter) increases from 30.06 to 2.21 × 10^5 kΩ following the onset of damage (Fig. 4(c)). After healing, the electrical resistance nearly returns to its original level due to the fusion of TPU during heating, which reconstructs the conductive pathway. Given its thermal deformation and flow

properties, TPU/MXene could be unevenly distributed during fracture and healing. This phenomenon may lead to a minor rise in resistance post-healing. The mechanical and electrical characteristics of STDF fibers were examined further under dynamic stretching conditions. During the stretching test under a harsh 10 % tensile strain, the electrical resistance increases by < 1 %, which is not significantly different from the change in fiber resistance before healing (Fig. 4(d)). To demonstrate the functionality, a light-emitting diode (LED) lamp was connected to a 6 V external power supply using STDF, which was entirely damaged and subsequently repaired (Fig. 4(e)). The LED lamp's brightness stays unchanged after healing, indicating a successful restoration of electrical properties.

The self-healing properties of STDF were carefully investigated under different healing conditions. Exploring the stress-strain curves after different healing times reveals that the tensile strength of STDF could reach 0.2 MPa (97.51 % of the initial value) after full damage and 24 h of healing (Fig. 4(f)). The fiber strength after 1–10 h of healing is close to the original fiber strength, because the fiber is in a relatively fragile state in the early stage of healing, and its internal structure and properties have not been fully restored. Reducing the healing time results in low healing efficiencies because the recovery of dynamic covalent is time-dependent networks [45]. Increasing the frequency of healing cycles (for example, repeating healing 1–5 times) slightly reduces healing efficiency, due to the chemical or physical degradation of the fiber during each healing cycle. To ensure the reliability of the experiment, this study conducted three independent experiments to test the healing efficiency of fibers before and after healing (Fig. S11). The results indicate that an increase in the number of healing cycles leads to a pronounced weakening of the healing interface, and unevenness results in stress concentration of fibers under stress, making them prone to fracture. Nevertheless, the mechanical healing efficiency of STDF can still reach 86.96 % after five healing cycles (Fig. 4(g)) due to the two main damage-induced physical cross-links present in the self-healing fiber, namely, the strong hydrogen bonds between TA and SA and reversible Schiff base bonds between C=O and NH_2 groups, and the weak Ca^{2+}-mediated ion complexation with SA (Fig. S12). In addition, Fig. 4(h) shows that after five cycles of stretching under different tensile strains (5 %, 10 %, 15 %, and 20 %), the strength that STDF can withstand remains unchanged, indicating its excellent mechanical stability after healing. These findings confirm the shell's efficient inner core protection and the mechanical-electrical connection between structural and conductive elements.

3.4. Flame retardancy and thermal stability of STDF fiber

Excellent thermal stability is essential for STDF. Fig. 5(a) and (b) and Table S5 show the TG and DTG curves of STDF at varying heating rates within a N_2 atmosphere. According to the TG and DTG curves, the weight loss range of coaxial fibers is 5 %–20 % at 30–200 °C. This part of the quality loss mainly comes from the adsorption of water, as the -OH of SA and the -NH_2 of SS absorb moisture, and OSA has a higher water absorption capacity than SA due to the hydrophilicity of aldehyde groups, resulting in more fiber quality loss in low-temperature regions. In addition, a small amount of residual EG on the surface of fibers can also lead to quality loss of fibers in low-temperature regions. 200–500 °C is the main stage of fiber decomposition, during which OSA sugar chains in the outer shell will break and SS peptide bonds will hydrolyze (temperature around 280 °C), but Ca^{2+} cross-linking can delay decomposition. When the temperature exceeds 500 °C, the fiber is in the high-temperature residual carbon stage. The Ca^{2+} cross-linked network helps promote the carbonization of organic components to produce residual $CaCO_3$ or CaO, thereby significantly enhancing the high-temperature resistance of fibers. In accordance with the Kissinger method, the temperature measurements (T_m) of STDF at varying heating rates of 10, 15, 20, and 30 K/min are recorded at 72, 81, 95, and 110 °C, respectively. The activation energy E of STDF can be determined by the slope between $\ln(\beta/T_m^2)$ and $1/T_m$, as shown in Fig. 5(c). According to the Kissinger method, the activation energy E of STDF is determined to be 291.25 kJ/mol. The pertinent data is encapsulated in Table S6. The Kissinger method is a simple method for quickly and roughly estimating E. However, this method only depends on the one-time maximum weight loss rate at each heating rate, and the calculated E is not accurate enough. To overcome this problem, the Flynn-Wall-Ozawa method is an effective strategy that calculates E through the relationship between $\lg\beta$ and $1/T$. The relationship between E and conversion rate α obtained through the Flynn-Wall-Ozawa method is shown in Fig. 5(d), and detailed data can be found in Table S7. The average activation energy, E_{ave}, calculated using the Flynn-Wall-Ozawa method, is 332.70 kJ/mol. Specifically, within the range of $\alpha \in (0.2, 0.4)$, as α increases from 0.3 to 0.4, E rises significantly before declining, suggesting that some intermediate products formed during thermal decomposition may enhance the thermal oxidation of polysaccharide biopolymers [46]. The E value experiences a slight rebound within $\alpha \in (0.4, 0.6)$. These findings imply that at this stage, increasing uncontrollable factors and specific undecomposed residues are influencing thermodynamic parameters. In this context, a high E indicates the superior thermal stability of the flame-retardant STDF.

In practical application scenarios, flame retardancy is crucial for STDF when used as a high-temperature warning sensor in wearable electronic textiles. The vertical burning test was performed to visually assess the flame-retardant effectiveness of STDF. The core fiber immediately ignites upon contact with the flame and burns out within 2 s, as shown in Fig. S13(a). By contrast, STDF does not catch fire and maintains its shape after being exposed to a flame for 6 s, suggesting that the shell fiber plays a crucial role in improving the flame resistance of STDF, thereby offering excellent protection to the flammable functional materials in the core layer (Fig. S13(b)). Additionally, the combustion characteristics of STDF were quantitatively evaluated further based on the heat release rate (HRR) and total heat release rate (THR), as presented in Fig. 5(e–g). The HRR curve indicates a swift rise in the HRR of STDF following ignition. Moreover, the peak HRR (pHRR) of STDF reaches 73.59 W/g, which is significantly lower than that of the core fiber (299.18 W/g, Fig. S14(a) and (b)). Similarly, Fig. 5(f) shows that the THR of STDF reaches 3.62 W/g, which is considerably lower than that of the core fiber (24.74 W/g). The above results indicate that the designed STDF with a core-sheath structure could remarkably reduce the heat released by the core fiber during combustion, thereby protecting the TE layer fibers and reducing the spread speed and hazard level of fires. The LOI test also obtained the same conclusion (Fig. 5(h)). The LOI value of the shell fiber is 38.8 %, indicating that it is a refractory material, whereas that of the core fiber, as a flammable material, is 16.1 %. The thoughtfully designed STDF has a core-sheath structure with a LOI of up to 29.8 %. This structure wraps the core fiber around the sheath layer, thereby reducing the direct contact between the core fiber and the external environment to a certain extent. It can form a protective layer during combustion, delaying or preventing the spread of flames to the core fiber and protecting it from damage. A comparison of pHRR reduction and LOI values (Fig. 5(i) and Table S8) demonstrates the superior flame-retardant properties of STDF over those of other fibers. The results indicate that STDF has higher pHRR reduction and LOI values than other bio-based aerogel fibers, surpassing even numerous flame-retardant-coated aerogels. Overall, the outstanding flame retardancy, lightweight nature, and thermal insulation capabilities of STDF create an excellent basis for

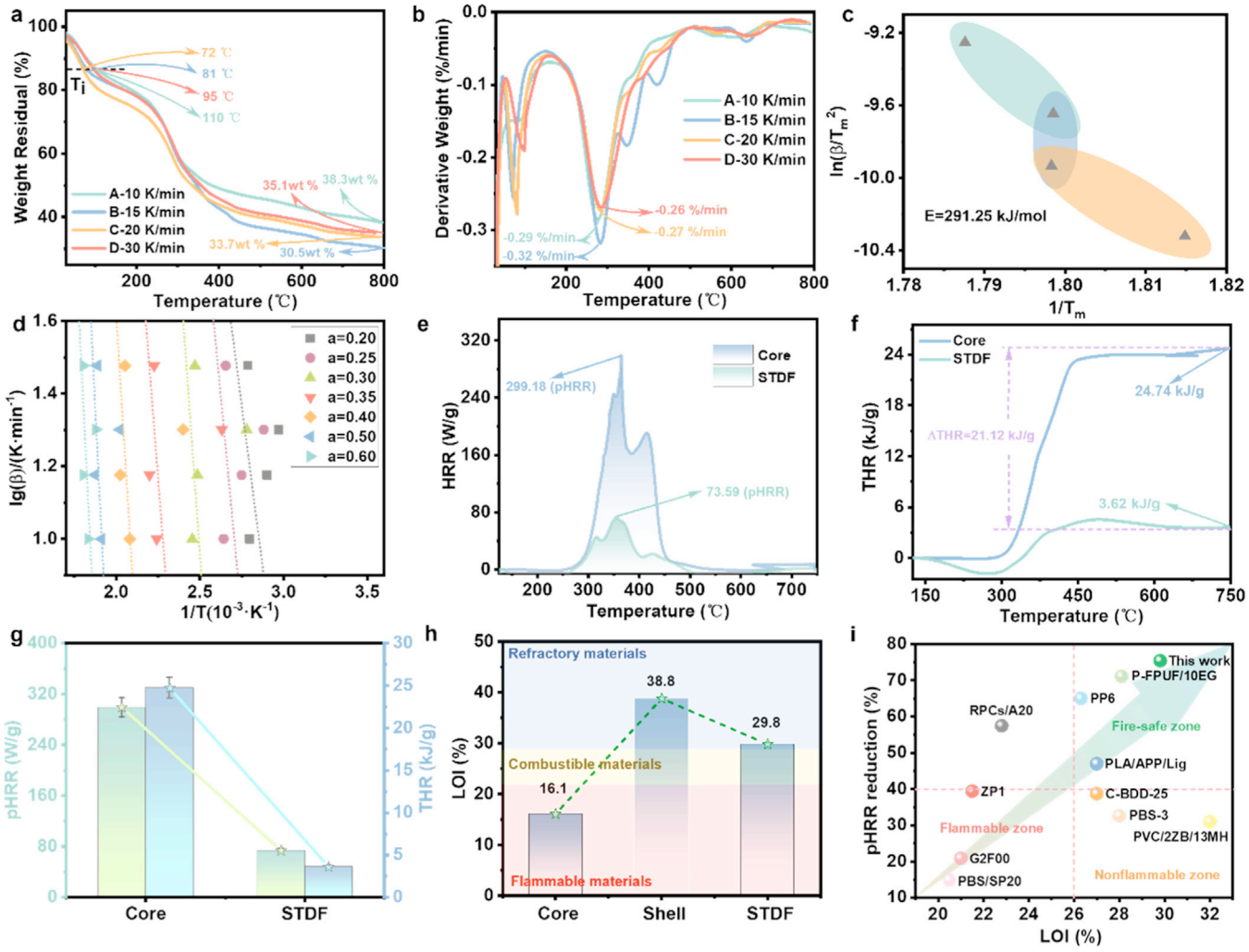

Fig. 5. Flame retardancy and thermal stability of STDF with autonomous self-healing and damage warning abilities. (a) TG and (b) DTG curves for STDF at various heating rates in a N_2 atmosphere. (c) Fitting lines of $\ln(\beta/T_m^2)$ against $1/T_m$ applying the Kissinger method. (d) Fitting lines of $\lg\beta$ against $1/T$ for various conversion rates using the Flynn-Wall-Ozawa method. (e) HRR and (f) THR curves of the core and STDF fiber. (g) Comparison of pHRR and THR changes between the shell fiber and STDF. (h) LOI values of the core and shell fibers and STDF. (i) Comparison of flame retardancy (LOI values and pHRR reduction) of the prepared STDF with other fibers from the literature (Table S8).

its application as a wearable self-powered high-temperature warning sensor.

3.5. Temperature sensing properties of STDF fiber

Fig. 6 illustrates the temperature-sensing capabilities of STDF. MXene, a novel 2D TE material, exhibits a favorable TE effect. When there is a temperature gradient across an MXene-based material, electrons shift from the heated side to the cooler side, creating a potential difference (Fig. S15). A homemade TE test platform was employed to evaluate the voltage changes in STDF at different temperatures. As illustrated in Figs. 6(a) and S16, two copper tapes were used to connect the two ends of the STDF TE fiber (five fibers in parallel) to the testing equipment, and two Peltier elements were employed to provide a stable temperature difference in STDF. When the Peltier elements are used for heating to generate a temperature difference of 25, 75, 125, and 175 K, the corresponding maximum output voltages of STDF are found to be 0.49, 0.10, 1.24, and 1.75 mV, respectively (Fig. 6(b)). The ability for direct conversion between the thermal and electrical energies of the resultant STDF primarily results from internal charge carriers migrating from the high-temperature area along the temperature gradient to the low-temperature area, thereby generating a potential difference. Fig. 6(c) and (d) demonstrate the output voltage and power of STDF as they relate to different temperature differences (ΔT). Maximum power occurs when external and internal resistances are equal [47]. The corresponding maximum power values are approximately 0.52, 2.14, 5.24, 9.68, and 15.34 μW for ΔT values of 20, 40, 60, 80, and 100 K, respectively. Fig. 6(e) depicts the fluctuation in the output voltage of STDF when it was subjected to varying temperatures (250–500 K), indicating the corresponding thermal voltage output related to various temperature differences. Under the protection of a flame-retardant shell, the TE functional particles MXene in the core layer can maintain structural stability at high temperatures [48], ensuring output voltage stability for effective temperature monitoring. Fig. 6(f) illustrates the correlation between the temperature difference across the temperature sensor and the resulting thermal voltage. The temperature difference exhibits a strong linear relationship with the output thermal voltage. This relationship can be described by the linear fitting function $U = 0.13113\Delta T + 0.00785$, which has a linear fit degree (R^2) of 0.99817.

Given the sensitive temperature-sensing performance of STDF, we fabricated an STDF-based e-textile (SFET; detailed information can be found in the experimental section) to design a self-powered high-temperature warning sensor. This sensor can be incorporated

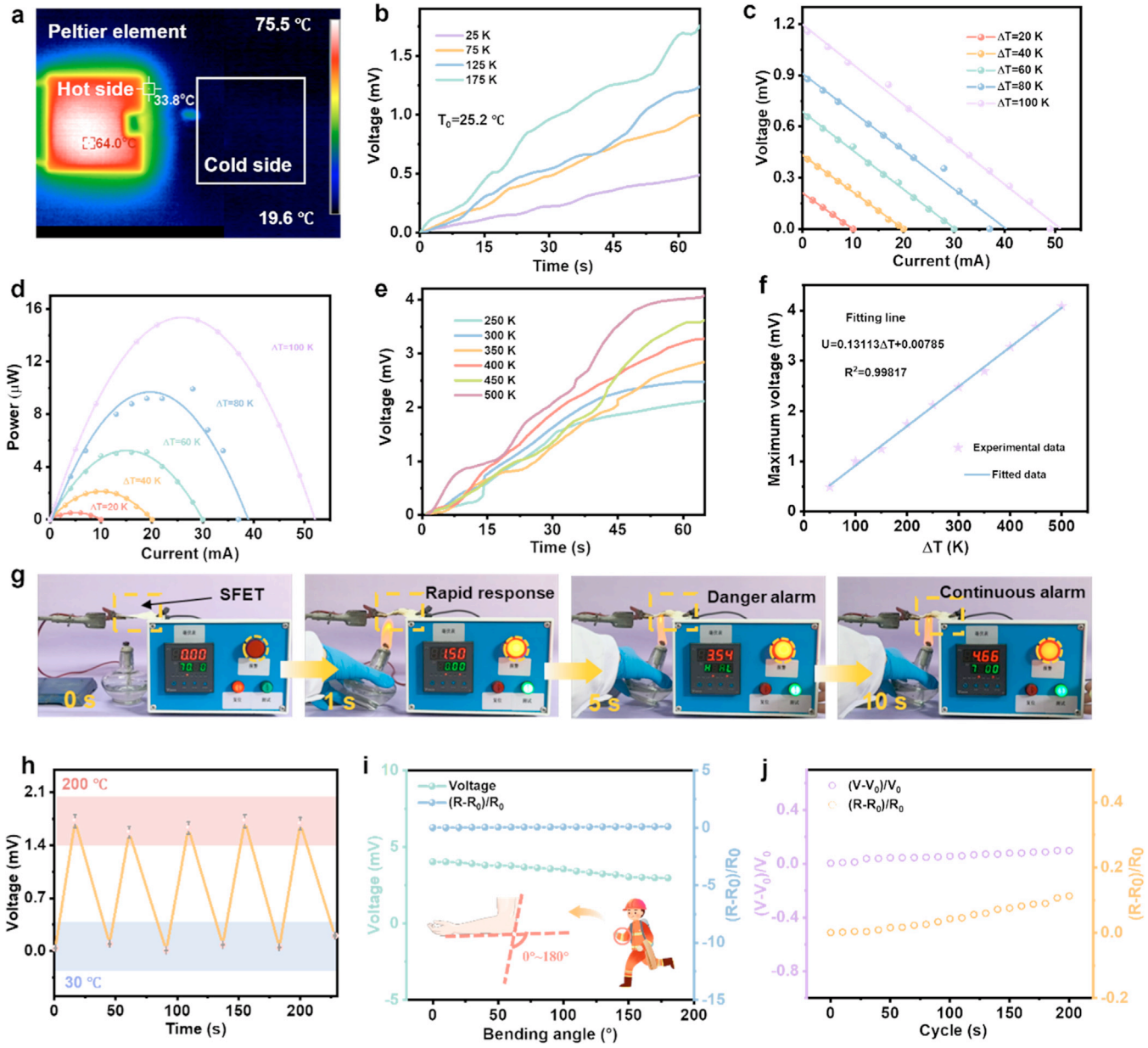

Fig. 6. Temperature-sensing performance of coaxial STDF with autonomous self-healing and damage warning abilities. (a) Infrared thermography of the Peltier-heated STDF. (b) Voltage variation curve over time measured by the Peltier element at different temperature differences. (c) Output voltage and (d) power of STDF with varying temperature differences (ΔT). (e) The output voltage of STDF varies when heated from 250 to 500 K, with room temperature at 25 °C. (f) ΔT of STDF showing a good linear relationship with the output thermal voltage. (g) High-temperature warning test on the SFET-based alarm sensor when in contact with an alcohol lamp flame. (h) Output voltage curves of SFET (three STDFs were sewn onto aramid fabric) over five cycles of heating to 200 °C and cooling to room temperature. (i) Resistance changes and output voltage of the SFET fabric-based sensor at different bending angles. (j) Impact of bending cycles on SFET resistance and output voltage at a 120° bending angle.

into firefighting clothing due to its excellent dynamic surface conformability, including the ability to withstand folding and bending features (Fig. S17). In this study, a triggering voltage of 1 mV was set for the high-temperature warning device. As illustrated in Fig. 6(g), the SFET activates the early high-temperature warning lamp in just 1.3 s when in contact with an alcohol lamp flame; this response time is significantly faster than that of commercial smoke and infrared fire alarm systems, which is approximately 100 s [48]. Furthermore, after several independent tests, SFET was exposed to flames for 5 cycles to more thoroughly explore its repeatable high-temperature alarm function (Fig. S18). Fig. S19 provides photographs of the repeated high-temperature warning tests on SFET. The findings indicate that the SFET-based high-temperature warning sensors can trigger the high-temperature alarm system in just 1.46 s upon exposure to an alcohol lamp flame again. When exposed to the flame for the fifth time, it only takes 9.25 s to trigger the warning system, which confirms the excellent stability and consistent high-temperature warning capabilities of SFET.

The TE fiber was subjected to five cycles of alternating heating (200 °C) and cooling (room temperature) to explore the repeatability and stability of the power generation performance of SFET (Fig. 6(h)). The highest output voltage of SFET at 200 °C remains consistent at approximately 1.72 mV after five repeated heating and cooling cycles. Considering that SFET-based self-powered high-temperature warning electronics are inevitably bent during wearing, the resistance changes of $(R - R_0)/R_0$ (where R_0 and R are the resistances before and after bending, respectively) and the output voltage were investigated at different bending angles from 0° to

180° at room temperature (Fig. 6(i)). The findings show that the resistance variation range is under 9.6 %, and the highest output voltage loss rate is 7.8 %. The resistance changes of $(R - R_0)/R_0$ and the output voltage changes of $(V - V_0)/V_0$ (where V_0 and V are the output voltages before and after bending, respectively) were measured after 200 cycles of bending at 120° to demonstrate the durability of STDF further (Fig. 6(j)). The findings indicate that voltage and resistance fluctuate by a maximum of 9.7 % and 9.3 %, respectively, after 200 bending-release cycles. This consistent performance in resistance and output voltage can largely be attributed to the durable protective shell fiber found in STDF. In addition, in order to adapt to more complex usage scenarios, this study conducted stability tests exposed to different humidity environments and chemical substances. The experimental results show that the resistance of STDF remains stable at 35.02 kΩ at a humidity of 10 %, and shows a linear decreasing trend as the humidity increases (Fig. S20(a)). This is because when the environmental humidity is too high, water molecules will intervene in the charge transfer path, and the fiber surface will adsorb water molecules to form a continuous conductive water film, providing additional electron transfer channels. Moreover, expose the fibers to different pH environments created by hydrochloric acid, water, and sodium hydroxide solutions to test their resistance changes (Fig. S20(b)). The experimental results confirm that the resistance change rate of STDF does not exceed 16 % at pH 6–8, indicating that the fiber has certain electrical stability in different acid-base environments. These results suggest that the excellent flexibility and durability of STDF present promising opportunities for developing flexible and reliable STDF-based high-temperature warning sensors.

3.6. Potential high-temperature warning application of the STDF in firefighting clothing

Firefighters wear firefighting uniforms as necessary protective equipment when carrying out firefighting operations, but the thermal decomposition of protective clothing can still cause burn incidents. Therefore, integrating STDF fibers with high-temperature warning capabilities into firefighting suits can warn firefighters to stay away from high-temperature flames before their suits are damaged by high temperatures, thereby enhancing operational safety. Fig. 7 illustrates the highly sensitive temperature monitoring performance of the SFET electronic textile-based temperature sensing device with a multistage wireless alarm system, which features independent damage alerts and self-healing capabilities. The potential application of STDF in SFET is demonstrated for providing assisted rescue communication to firefighters (Fig. 7(a)). Firefighting clothing with integrated temperature sensing electronic textiles could enable firefighters to share information comfortably due to its wearability. The STDF-based high temperature alarm sensor acts as a self-sufficient signal conversion module, producing voltage signals in response to high temperatures to trigger high temperature warning systems without needing extra electronic parts or energy supply units (Fig. 7(b)). The signal acquisition module of a microcontroller linked to the transmitter captures the voltage signal to indicate temperature variations. Fig. 7(b) illustrates the design of the multistage wireless alarm system, which consists of three modules: an energy collection unit, an energy transmission unit, and a wireless microcontroller unit (Figs. S21–S24). Based on the previously described concepts, precise wireless detection equipment was constructed for verification purposes. Additionally, the system was effectively tested using Peltier elements with temperature-triggered adjustable voltage thresholds to validate its performance at elevated temperatures (Fig. S25). The signal transmitter was integrated into a firefighting suit and located far from the signal receiver. In the absence of high temperatures (below 200 °C), the wireless signal displays a green light, indicating that the surrounding environment is safe for firefighters. However, once a high temperature (200–400 °C) is detected, the alarm system triggers an orange alarm light, warning firefighters that the ambient temperature is gradually increasing and that they must remain alert to high-temperature flames at all times. When the temperature exceeds 400 °C, a red light turns on, indicating that firefighters must evacuate immediately to ensure their safety.

The durability of SFET was evaluated through a series of bending, twisting, and tensile tests. Fig. S26(a) and (b) illustrates the results of eight and 50 cyclic tensile tests on the SFET samples, respectively. The maximum tensile strength of SFET is 63.81 MPa at 10 % strain. After 50 cyclic tensile tests, the tensile strength of SFET could still reach 58.77 MPa, which is 92.10 % of the initial strength. During stress monitoring, the resistance change of SFET was also recorded under 50 cycles of cyclic stretching. Fig. S26(c) illustrates the variations in the resistance of SFET during cyclic stretching. The release deformations at 10 % lateral strain do not exceed ±0.5 %, indicating that SFET is highly electrically reliable. The stress and resistance after three tensile cycles before and after healing were compared to verify the durability of SFET after healing (Fig. 7(c) and (d)). The results show that the maximum strength of SFET before healing is 68.63, 66.228, and 63.935 MPa from cycle 1 to cycle 3. However, strength slightly decreases after healing (efficiency remains at approximately 78 %), with the maximum strength from cycle 1 to cycle 3 being 54.09, 51.86, and 49.92 MPa. Nevertheless, the decrease in the strength of SFET after healing is a normal phenomenon because the changes in fiber properties after healing may be related to the loss of dynamic bonds. Dynamic bonds need to absorb energy to break and release energy during healing to regenerate. During this process, some energy may be lost in the form of thermal or other forms of energy, resulting in the loss of dynamic bonds. In addition, the resistance change of SFET after healing is almost no >0.3 %. Fig. S27 tests the fiber water splitting absorption curve at the beginning of water-driven self-healing. The results indicate that the fiber moisture content can completely return to zero within 2.3 h, indicating that the fiber does not contain moisture after complete healing. Therefore, the water-driven healing method has no effect on the long-term function of the fiber. This result further confirms that SFET still has excellent performance after STDF fiber healing. The same conclusion can be drawn in the bending and twisting experiments on SFET. When bent at 72°, the resistance of SFET after healing fluctuates slightly compared with that before healing; overall, the relative change in resistance does not exceed 0.4 % (Figs. 7(e) and S28). In addition, in the torsion experiment, the stress curve of SFET is stable, demonstrating the excellent mechanical durability of SFET (Figs. 7(f) and S29). Furthermore, to verify the reliability of SFET applied to firefighting clothing, the warning performance of SFET was tested after five washes and drying (Fig. S30). The experimental results demonstrate that SFET can still trigger the warning system within 2.5 s after washing, with a triggering voltage change rate not exceeding 7 %. Therefore, the SFET prepared in this study has excellent mechanical stability and reliability when integrated into firefighting clothing.

Additionally, this study developed a concept to use the large-area e-textile SFET for high-temperature warning in smart firefighting suits with a multistage wireless alarm system. When a firefighter outfitted in this SFET textile enters a high-temperature environment, the intelligent fabric harnesses surrounding heat energy. This process activates the SFET, allowing it to visualize the heated zone and send out wireless sensing signals triggered by the discharge (Fig. 7(g)). It was demonstrated that the receiver can also detect the wireless heat signal and utilize it to manage indoor electronics (Fig. 7(h)). The integration of SFET into firefighting gear allows for the detection of the suit's surface temperature, enabling immediate alerts for firefighters to evacuate before any

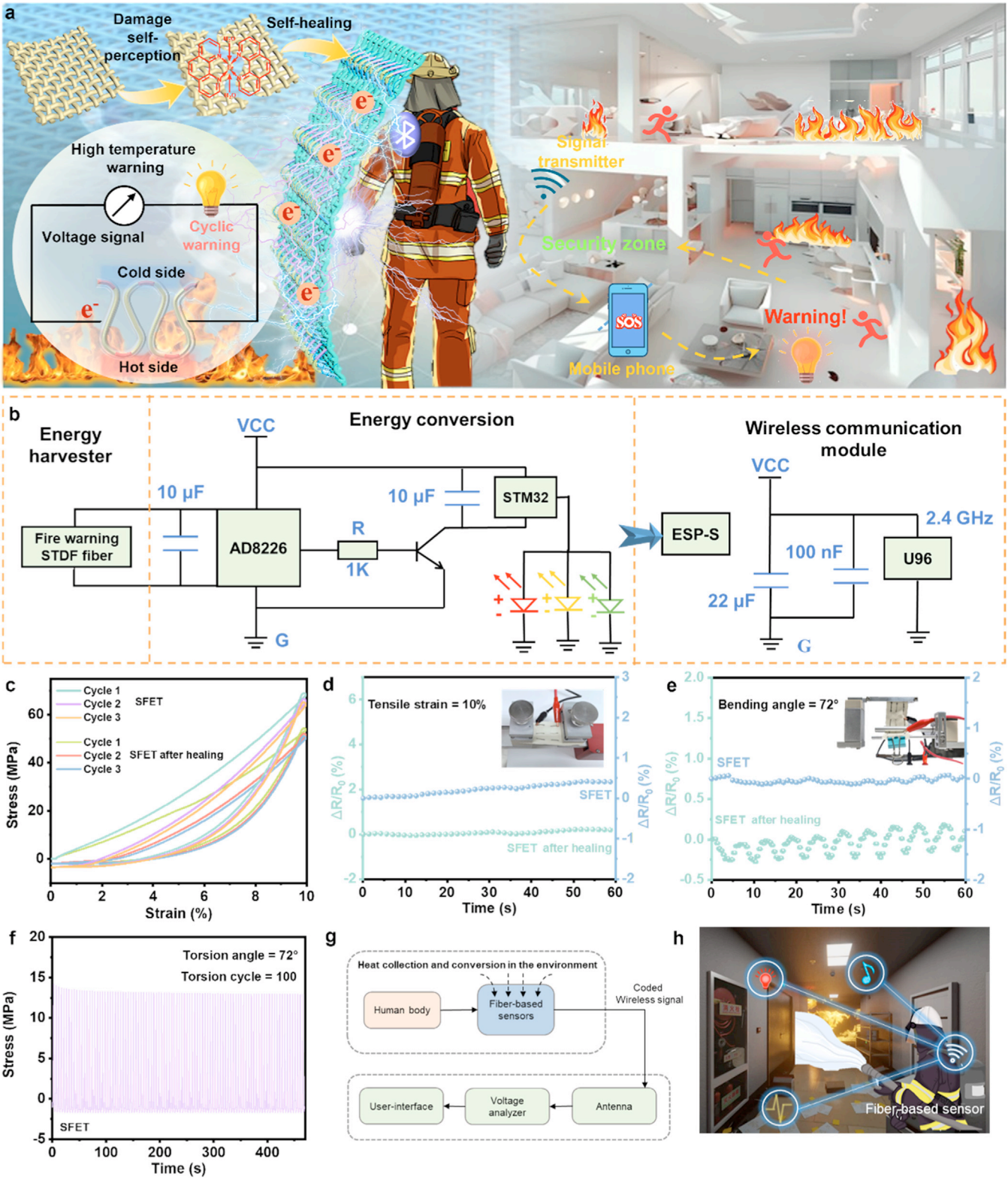

Fig. 7. Extended application of the SFEF with a multistage wireless alarm system for high-temperature warning in firefighting clothing. (a) A diagram illustrating a high-temperature alarm system integrated with SFET within firefighting suits. (b) Schematic of the SFET-based self-powered, autonomously operating multistage wireless high temperature alarm system. (c) Tensile stress-strain curve of SFET after three cycles of stretching before and after healing. (d) Resistance change rate of SFET after 10 cycles of cyclic stretching before and after healing (tensile strain of 10 %). (e) Resistance change rate of SFET after 100 cycles of bending before and after healing (bending angle of 72°). (f) Stress changes in SFET after 100 torsion cycles before and after healing (torsion angle of 72°). (g) Schematic representation of smart firefighting suits based on STDF. (h) Possible use of STDF-based textiles in fire situations.

malfunction occurs. Additionally, if SFET encounters flame or excessive heat, a wireless detection system transmits a fire warning to an operator monitoring temperature and voltage levels from a remote site. When temperatures surpass 400 °C, and the threshold for warnings (0.99 mV) is triggered, the wireless transmitter sends a signal to the receiver. This activation triggers an alarm with a light signal to prompt firefighters to evacuate immediately.

4. Conclusions

In summary, we propose a biomimetic design strategy for core-sheath structure temperature sensing aerogel fiber integrating self-healing and visual damage location function through a coaxial wet spinning strategy. This strategy yields a core-shell heterogeneous structure STDF aerogel fiber with an intrinsic self-healing protective sheath and a temperature-sensing core layer. The unique eggshell structure assembly, cross-linked by Ca^{2+}, contains numerous noncovalent binding sites on its surface. These sites enable the construction of hydrogen and metal coordination bonds with the spherical-arranged branch units (-OH) from TA. The combination of multiple dynamic cross-linking networks provides a promising method for improving the limited service life of biopolymers. The coaxial fiber exhibits fatigue-free yet self-warning damage and autonomous healing abilities through the synergy between multiple hydrogen bonds and Schiff base dynamic covalent bonds, resembling visual bleeding warning and a self-healing mechanism. Such a design affords an optimum efficiency of 97.51 % while maintaining visual damage warning and precise healing abilities. Moreover, the obtained STDF exhibits outstanding tensile strength, preserving its original mechanical strength after stretching, bending, and twisting 100 times. It also demonstrates excellent repetitive mechanical recovery healing ability (86.96 %) even after five damage-healing cycles. In addition, the innovative STDF derived from the flame-retardant shell-TE core structure can be used as a self-powered high-temperature warning sensor and exhibits favorable functional reliability over a wide temperature range (100–500 °C). Finally, the temperature-sensing electronic textile based on STDF TE fiber could expand the field of application in next-generation wearable flexible electronics, given its high structural stability and functional reproducibility after damage.

Declaration of competing interest

The authors declare that they have no known competing financial interests or personal relationships that could have appeared to influence the work reported in this paper.

CRediT authorship contribution statement

Hualing He: Conceptualization, Investigation, Writing – original draft. **Qing Jiang:** Data curation, Investigation, Writing – original draft. **Yuhang Wan:** Validation. **Md Hasib Mia:** Formal analysis. **Xueru Qu:** Data curation. **Mi Zhou:** Resources. **Xingyu He:** Validation. **Xiaoqian Li:** Visualization. **Min Hong:** Validation. **Zhicai Yu:** Supervision, Writing – review & editing, Conceptualization, Funding acquisition. **Siqi Huo:** Supervision, Writing – review & editing.

Acknowledgments

This work was financially supported by the Wuhan Textile University School Fund (B) (No. k24016). Thanks to Shiyanjia Lab (www.shiyanjia.com) for the testing services.

Supplementary materials

Supplementary material associated with this article can be found, in the online version, at doi:10.1016/j.jmst.2025.06.038.

References

[1] B.H. Jia, D. Wu, L. Xie, W. Wang, T. Yu, S.Y. Li, Y. Wang, Y.J. Xu, B.B. Jiang, Z.Q. Chen, Y.X. Weng, J.Q. He, Science 384 (2024) 81–86.
[2] H.L. Yu, Z.Q. Hu, J. He, Y.J. Ran, Y. Zhao, Z. Yu, K.P. Tai, Nat. Commun. 15 (2024) 2521.
[3] C.G. Han, X. Qian, Q.K. Li, B. Deng, Y.B. Zhu, Z.J. Han, W.Q. Zhang, W.C. Wang, S.P. Feng, G. Chen, W.S. Liu, Science 368 (2020) 1091–1098.
[4] B.Y. Yu, J.J. Duan, H.J. Cong, W.K. Xie, R. Liu, X.Y. Zhuang, H. Wang, B. Qi, M. Xu, Z.L. Wang, J. Zhou, Science 370 (2020) 342–346.
[5] J.Y. Xiao, Z. Zhang, Z.X. Liao, J.Z. Huang, D.X. Xian, R.H. Zhu, S.C. Wang, C.M. Gao, L. Wang, J. Mater. Sci. Technol. 207 (2025) 246–254.
[6] R. Dhawan, P. Madusanka, G.Y. Hu, J. Debord, T. Tran, K. Maggio, H. Edwards, M. Lee, Nat. Commun. 11 (2020) 4362.
[7] Z.C. Yu, L.L. Huang, M. Zhou, J. Xu, J.C. Ma, Y.H. Wan, Q. Jiang, X.R. Qu, H.L. He, Chem. Eng. J. 512 (2025) 162586.
[8] Z.C. Yu, Y.H. Wan, M. Zhou, M.H. Mia, S.Q. Huo, L.L. Huang, J. Xu, Q. Jiang, Z.R. Zheng, X.D. Hu, H.L. He, Nano-Micro. Lett. 17 (2025) 214.
[9] W.Y. Wang, D.J. Yao, H. Wang, Q.L. Ding, Y.B. Luo, H.J. Ding, J.H. Yu, H. Zhang, K. Tao, S. Zhang, F.W. Huo, J. Wu, Adv. Funct. Mater. 34 (2024) 2316339.
[10] M.W. Zhang, R. Yu, X.L. Tao, Y.Y. He, X.P. Li, F. Tian, X.Y. Chen, W. Huang, Adv. Funct. Mater. 33 (2023) 2208083.
[11] M.H. Mia, Y.H. Wan, Q. Jiang, L.L. Huang, M. Zhou, J. Xu, X.L. Gong, X.D. Hu, Z.C. Yu, H.L. He, Carbohydr. Polym. 358 (2025) 123563.
[12] Z.Y. Hui, L.R. Zhang, G.Z. Ren, G.Z. Sun, H.D. Yu, W. Huang, Adv. Mater. 35 (2023) 2211202.
[13] D.Y. Wang, L.L. Wang, Z. Lou, Y.Q. Zheng, K. Wang, L.J. Zhao, W. Han, K. Jiang, G.Z. Shen, Nano Energy 78 (2020) 105252.
[14] Y. Guo, Q.S. Yang, S.Q. Huo, J. Li, P. Jafari, Z.P. Fang, P.A. Song, H. Wang, Prog. Polym. Sci. 162 (2025) 101935.
[15] A.L. Zhang, J.Z. Zhang, L.N. Liu, J.F. Dai, X.Y. Lu, S.Q. Huo, M. Hong, X.H. Liu, M. Lynch, X.S. Zeng, P. Burey, P.A. Song, J. Mater. Sci. Technol. 167 (2023) 82–93.
[16] H.G. Yue, Y. Wang, S.C. Luo, J.F. Guo, J. Jin, G.X. Li, Z.H. Meng, L. Zhang, D.S. Zhou, Y.G. Zhen, W.P. Hu, Sci. Adv. 10 (2024) eadq0171.
[17] W.L. Li, X.C. Lu, J.M. Diamond, C.T. Shen, B. Jiang, S. Sun, J.S. Moore, N.R. Sottos, Nat. Commun. 15 (2024) 2771.
[18] X.B. Xi, T. Ye, S. Wang, X.M. Na, J.H. Wang, S. Qing, X.Y. Gao, C.L. Wang, F. Li, W. Wei, G.H. Ma, Sci. Adv. 6 (2020) eaay7735.
[19] S. Marchesan, Nature 630 (2024) 308–309.
[20] T. Yimyai, D. Crespy, M. Rohwerder, Adv. Mater. 35 (2023) 2300101.
[21] Z.W. Ma, J.B. Feng, S.Q. Huo, Z.Q. Sun, S. Bourbigot, H. Wang, J.F. Gao, L.C. Tang, W. Zheng, P.A. Song, Adv. Mater. 36 (2024) 2410453.
[22] M.M. Zhu, J.L. Li, J.Y. Yu, Z.L. Li, B. Ding, Angew. Chem. Int. Ed. 61 (2022) 202200226.
[23] Y. Wan, X.C. Li, H.T. Yuan, D.X. Liu, W.Y. Lai, Adv. Funct. Mater. 24 (2024) 2316550.
[24] C. Chen, T. Shen, J. Yang, W.K. Cao, J.H. Wei, W.H. Li, Chem. Eng. J. 498 (2024) 155158.
[25] H.J. Gong, Y. Song, G.L. Li, L. Zhang, D. Guo, G.X. Xie, Compos. Pt. B-Eng. 260 (2023) 110776.
[26] J.A. Capets, S.F. Yost, B.D. Vogt, C.W. Pester, Adv. Funct. Mater. 34 (2024) 2406277.
[27] J.M. Jin, C.C. Sun, K.Y. Xu, X.L. Sun, L.L. Cao, L.L. Liu, Int. J. Biol. Macromol. 261 (2024) 129734.
[28] C.S. Yu, X.K. Li, X. Yang, X.Y. Qiu, X.X. Zhang, Z.M. Chen, Y.L. Luo, Small 20 (2024) 2311656.
[29] L.M. Liu, S.L. Chen, Y. Hu, W. Pan, T.Y. Dong, Y.F. Chen, L. Lin, L.Q. Wang, Adv. Funct. Mater. 34 (2024) 2404760.
[30] H. Wu, Z.L. Zhu, N.J. Gao, L. Ma, J.W. Li, F.C. Liu, Nano Res. 16 (2023) 10587–10596.
[31] H.D. Bai, Y.S. Kim, R.F. Shepherd, Sci. Adv. 8 (2022) eabq2104.
[32] Z. Li, Y. Zhang, S.Q. Huang, X.X. Wu, L. Shi, Q. Liu, J. Nanopart. Res. 22 (2020) 334.
[33] H.L. He, Y.S. Wang, Z.C. Yu, J.R. Liu, Y.H. Zhao, Y.S. Ke, Carbohydr. Polym. 269 (2021) 118291.
[34] S. Wang, X.Y. Fan, Z.X. Zhang, Z. Su, Y.N. Ding, H.Y. Yang, X. Zhang, J.Z. Wang, J. Zhang, P.A. Hu, ACS Nano 18 (2024) 17175–17184.
[35] Y. Lee, J. Park, A. Choe, S. Cho, J. Kim, H. Ko, Adv. Funct. Mater. 30 (2020) 1904523.
[36] B. Gurzeda, N. Boulanger, A. Nordenström, C. Dejoie, A.V. Talyzin, Adv. Sci. 11 (2024) 2408448.
[37] H.L. He, Y. Qin, Z.Y. Zhu, Q. Jiang, S.N. Ouyang, Y.H. Wan, X.R. Qu, J. Xu, Z.C. Yu, Nano-Micro Lett. 15 (2023) 226.
[38] S. Seyedin, S. Uzun, A. Levitt, B. Anasori, G. Dion, Y. Gogotsi, J.M. Razal, Adv. Funct. Mater. 30 (2020) 1910504.
[39] Q. Jiang, Y.H. Wan, Y. Qin, X.R. Qu, M. Zhou, S.Q. Huo, X.C. Wang, Z.C. Yu, H.L. He, Adv. Fiber Mater. 6 (2024) 1387–1401.
[40] J. Li, J. Han, W. Yu, K. Wang, Z. Liu, Y. Liu, Int. J. Biol. Macromol. 242 (2023) 124886.
[41] X.J. Chen, H.A. Wang, H.F. Hu, Y.X. Feng, L.P. Tian, W.C. Shi, H.G. Liang, Y.S. Yang, Q.F. Sun, Y.Y. Li, Sep. Purif. Technol. 337 (2024) 126399.
[42] Y.X. Ma, Y. Ma, Z. Yu, B.S. Chiou, F. Liu, F. Zhong, Food Hydrocoll. 124 (2022) 107340.
[43] C.F. Guo, Y. Gao, S.Q. Li, Y.X. Wang, X.J. Yang, C.W. Zhi, H. Zhang, Y.F. Zhu,

S.Q. Chen, S.L. Chou, S.X. Dou, Y. Xiao, X.P. Luo, Adv. Funct. Mater. 34 (2024) 2314651.
[44] H.L. Lin, X.Y. Chen, H. Lei, X.J. Zhou, G.B. Du, H. Essawy, X.D. Xi, D.F. Hou, J.X. Song, M. Cao, Int. J. Biol. Macromol. 264 (2024) 130020.
[45] S. Wang, Z.F. Ouyang, S.T. Geng, Y. Wang, X.J. Zhao, B. Yuan, X. Zhang, Q.C. Xu, C.Q. Tang, S.S. Tang, H. Miao, H.S. Peng, H. Sun, Natl. Sci. Rev. 11 (2024) nwae006.
[46] T. Sai, X.D. Ye, B.T. Wang, Z.H. Guo, J. Li, Z.P. Fang, S.Q. Huo, J. Mater. Sci. Technol. 225 (2025) 11–20.
[47] C. Kwon, S. Lee, C. Won, K.H. Lee, M. Kim, J. Lee, S.J. Yang, M. Lee, S. Lee, K. Yoon, S. Cho, T. Lee, Adv. Funct. Mater. 33 (2023) 2300092.
[48] H.L. He, Y. Qin, J.R. Liu, Y.S. Wang, J.F. Wang, Y.H. Zhao, Z.Y. Zhu, Q. Jiang, Y.H. Wan, X.R. Qu, Z.C. Yu, Chem. Eng. J. 460 (2023) 141661.